



# Stress-adapted fiber orientation along the principal stress directions for continuous fiber-reinforced material extrusion

Tim Heitkamp<sup>1</sup> · Sebastian Kuschmitz<sup>2</sup> · Simon Girnth<sup>1</sup> · Justin-Dean Marx<sup>1</sup> · Günter Klawitter<sup>1</sup> · Nils Waldt<sup>1</sup> · Thomas Viotor<sup>2</sup>

Received: 17 March 2022 / Accepted: 15 September 2022  
© The Author(s) 2022

## Abstract

A proven method to enhance the mechanical properties of additively manufactured plastic parts is the embedding of continuous fibers. Due to its great flexibility, continuous fiber-reinforced material extrusion allows fiber strands to be deposited along optimized paths. Nevertheless, the fibers have so far been embedded in the parts contour-based or on the basis of regular patterns. The outstanding strength and stiffness properties of the fibers in the longitudinal direction cannot be optimally utilized. Therefore, a method is proposed which allows to embed fibers along the principal stresses into the parts in a load-oriented manner. A G-code is generated from the calculated principal stress trajectories and the part geometry, which also takes into account the specific restrictions of the manufacturing technology used. A distinction is made between fiber paths and the matrix so that the average fiber volume content can be set in a defined way. To determine the mechanical properties, tensile and flexural tests are carried out on specimens consisting of carbon fiber-reinforced polyamide. In order to increase the influence of the principal stress-based fiber orientation, open-hole plates are used for the tensile tests, as this leads to variable stresses across the cross section. In addition, a digital image correlation system is used to determine the deformations during the mechanical tests. It was found that the peak load of the optimized open-hole plates was greater by a factor of 3 and the optimized flexural specimens by a factor of 1.9 than the comparison specimens with unidirectional fiber alignment.

**Keywords** Fiber reinforced additive manufacturing · Design for additive manufacturing · Material extrusion · Principal stress · Curvilinear fiber · Continuous fiber

## 1 Introduction

Material extrusion (MEX) is characterized by the production of parts by continuous layer-by-layer application of a molten thermoplastic strand. The initial material is usually in the form of a thermoplastic filament, which can be continuously unwound from a filament spool [1, 2]. In the past, the MEX process was primarily used for the fast and cost-effective production of prototypes. However, further developments of the process and the materials used have led to an increasing number of end products being manufactured using the process [2]. The layer-by-layer process principle enables the

economical production of arbitrarily complex components directly from 3D CAD data without significant additional effort. However, this leads to anisotropic material properties with poorer mechanical properties in the build-up direction [2, 3]. Thus, the MEX process is often ruled out when selecting suitable manufacturing processes for production in industrial practice, since the mechanical properties of the manufactured parts are rarely sufficient for the load case at hand [3]. In addition to pure thermoplastics, filaments with added fillers can also be processed to improve the strength of parts. In this context, fillers in the form of reinforcing fibers are primarily suitable [3–5]. A comparatively simple approach is the use of short fiber reinforced filaments [6]. Fibers with a length of 0.1–1 mm are added to the thermoplastic filaments. Thus, the filaments can be processed with conventional extruders. In general, short fiber reinforcement improves the tensile and flexural strength and stiffness of the parts, while it reduces the toughness, yield strength and ductility [7–10]. Due to the significantly improved mechanical

✉ Tim Heitkamp  
tim.heitkamp@hs-hannover.de

<sup>1</sup> Hochschule Hannover, 30459 Hannover, Germany

<sup>2</sup> Institute for Engineering Design, Technische Universität Braunschweig, 38108 Braunschweig, Germany

properties compared to short fiber reinforcements, continuous fibers are increasingly used for additive manufacturing of fiber-reinforced thermoplastic parts [11, 12]. Due to their high strength and stiffness values, carbon, glass or aramid fibers are preferably used as reinforcing fibers. Two different approaches have been established for embedding continuous fibers in parts manufactured by MEX, which differ in the timing of fiber impregnation (see Fig. 1). One approach is to impregnate the fibers during the process within the extruder. Accordingly, the fibers are initially in the form of rovings. In the print head, the supplied fiber strand bonds with the molten filament and is deposited together on the part (see Fig. 1a). This approach has already been studied and demonstrated in various research papers [13–18]. Another concept involves fiber impregnation prior to the process. For this purpose, semi-finished products consisting of a thermoplastic matrix and continuous fibers embedded therein are used, which are applied to the print bed or the part with an extruder (see Fig. 1b) [13, 19].

The use of continuous fiber reinforcements leads to a significant increase in the strength of the parts. The mechanical properties of continuous fiber reinforced parts fabricated using different approaches and materials have been described in detail in numerous studies [14–17, 20–24]. The mechanical properties obtained depend on a number of factors. In addition to the basic process parameters, the fiber and matrix materials, fiber volume fraction, interfacial adhesion and the number of defects in the part also influence the mechanical properties [25]. Delamination and fiber-matrix debonding have been shown to be the main failure mechanisms in various studies [16, 26–28]. Another decisive factor for the mechanical properties is the fiber orientation in the parts. Parts reinforced with continuous fibers exhibit many times higher strength and

stiffness properties in the fiber direction than across the fiber direction. Due to this extreme anisotropy in the fiber direction, fiber-reinforced plastics offer enormous lightweight design potential when the fibers are aligned in line with the load.

For manufacturing using MEX, a G-code (a machine code readable by the 3D printers [29, 30]) is required. The G-code is generated during the slicing process. In the slicing process, the 3D part geometry is first loaded into the slicing software and the build orientation is defined. Then the part is sliced into layers and divided into outer and inner contours (perimeters) and an inner regular infill pattern. The perimeters and infill patterns correspond to the tool paths to be traced by the print head [2]. Manufacturers of fiber printing systems, such as Markforged [31] and Anisoprint [32], also offer corresponding slicing software (Markforged–Eiger [33], Anisoprint–Aura [34]) for their respective systems, which allows slicing of parts and creation of tool paths for the pure thermoplastic and for the continuous fiber strands. These are user-friendly slicing programs that specify optimized process parameters that can be varied only to a very limited extent. Various options are available in the slicing software for fiber alignment. These are, for example, contour-based, unidirectional or rhombic infill patterns (see Fig. 2), which are comparable to the infill patterns of conventional MEX. However, the embedded fiber strands are of particular importance with regard to the mechanical properties. Due to the anisotropic properties, fiber orientation adapted to the load is essential. With existing slicing programs, however, the fibers are placed in the part on the basis of regular patterns. Load-adapted fiber placement based on numerical simulation methods is not possible with conventional slicing programs.

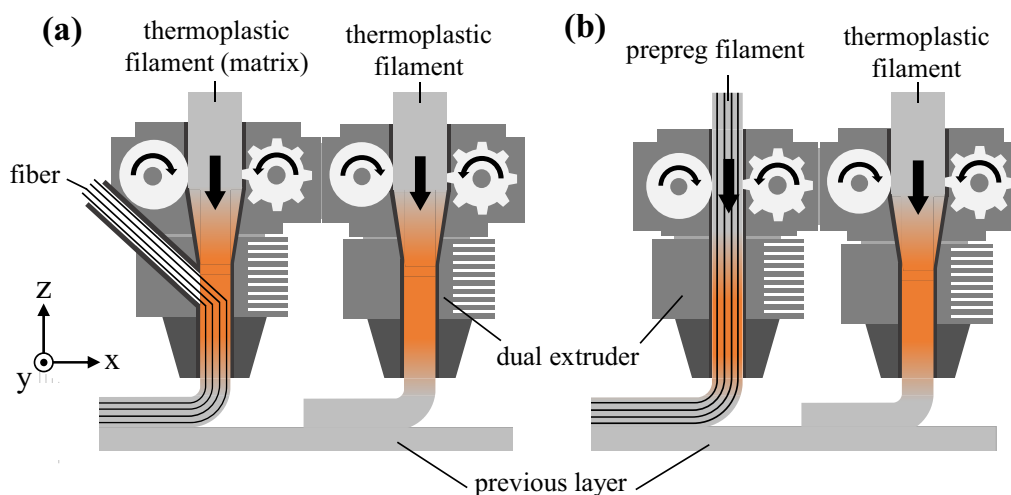


**Fig. 1** Schematic representation of the approaches for the insertion of continuous fibers in the MEX process

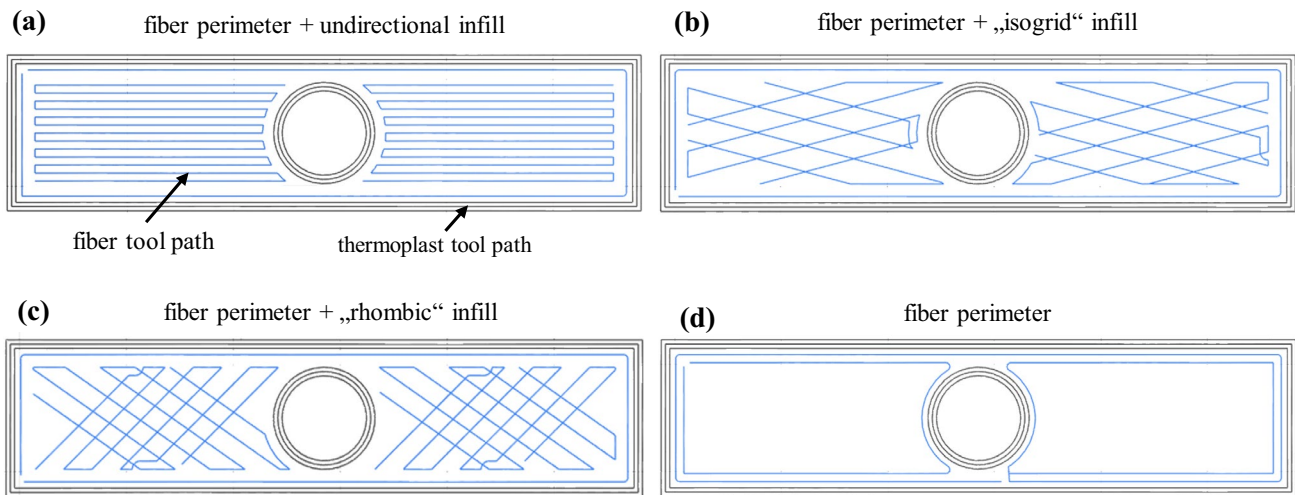


**Fig. 2** Exemplary infill patterns with continuous fibers generated with the slicing software Aura (Anisoprint [34]), fiber perimeter with unidirectional infill in (a), with “isogrid” infill in (b), with “rhombic” infill in (c) and without additional fiber infill in (d)

### 1.1 Stress-adapted fiber placement

In recent years, various approaches have been pursued to introduce fibers into the part in a way that is appropriate to the load. By means of numerical methods, it could be shown that a load-appropriate alignment of the fibers can lead to a significant improvement of the mechanical properties. Zhang et al. [35] used FE analyses and streamtracer plots to generate fiber orientations based on principal stress tensors. In the numerical calculations, the optimized orientation resulted in a significant reduction in stress peaks compared to  $90^\circ/0^\circ$  and  $45^\circ/-45^\circ$  multilayer composites.

Malakhov and Polilov [36] also used numerical methods to calculate load-oriented fiber orientations in order to be able to adapt fiber paths to geometric discontinuities, such as notches or holes, in an optimized manner. A principal stress-oriented infill pattern resulted in a 3.2-fold reduction in stress peaks compared to the straight fiber orientations in the numerical model.

Malakhov et al. [37] presented an iterative simulation-based method to calculate the fiber paths in order to manufacture parts with variable stiffnesses. In the simulations, the optimized fiber orientation resulted in a 6 times improvement in stiffness compared to unidirectional fiber orientation. The iterative simulation method for adjusting variable stiffnesses was practically investigated by Sugiyama et al. [38]. The effects of the optimized fiber alignment on the mechanical properties of a fiber paths uniformly surrounding the hole on one side, the stiffnesses could be increased by factors of 4.5 and 9.4, respectively. The maximum load capacity of the open-hole plates could be increased by a factor of 1.2 and 1.6, respectively.

Li et al. [39] generated load-path appropriate tool paths for fiber insertion in printed composite parts. The load paths are based on the tensile and compressive stresses occurring in the part. The mechanical tests were carried out on continuous fiber-reinforced open-hole plates. The optimized infill patterns showed 67.5% and 62.4% higher tensile and flexural strengths, respectively, than the conventional straight infill patterns. The strength-to-weight ratio of the optimized tensile and flexural specimens exceeded the conventionally specimens by 55.1% and 35.2%, respectively.

The mechanical properties of open-hole tensile specimens made of continuous fiber-reinforced thermoplastic were investigated by Hou et al. [40]. Optimized fiber orientation was based on stress gradients. Comparisons with unidirectional fiber orientation increased the ultimate strength by 42% and reduced the stress concentration by 36%.

### 1.2 Aims and scope

The aim of this work is to develop a method for the stress-adapted design and manufacturing of continuous fiber-reinforced components using MEX in order to improve the mechanical properties of the components. In contrast to existing approaches, computer aided internal optimization (CAIO) is used for fiber reinforced MEX for the first time to the best of the authors' knowledge. With the aid of this method, it is possible to precisely determine the principal stress trajectories with any number of flexibly selectable starting points. The CAIO method allows effortless adaptation of any number of trajectories even for complex part geometries. In addition, the method allows the generation and selection of defined fiber trajectories without recalculations, which is a disadvantage in other simulation-based

methods [41]. The plotted principal stress trajectories can be used directly as fiber toolpaths. Accordingly, the fibers strictly follow the principal stress directions.

To validate the method, solid specimens with embedded continuous fiber strands are fabricated. On the one hand, open-hole plates are used as specimens, for which only the first principal stress direction is taken into account. In addition, flexural specimens with layerwise alternating fiber paths along the first and second principal stress directions were printed and tested. Mechanical tests on optimized and unidirectional reinforced specimens will show the impact on the mechanical properties. In addition, it will be investigated whether the principal stress-based fiber orientations differ from unidirectional fiber orientations in terms of failure mechanisms.

## 2 Principal stress-based fiber alignment

Compared to conventional isotropic materials, the anisotropic properties and high specific strengths of the reinforcing fibers offer considerable potential for lightweight construction applications, especially when aligned to withstand loads. Fibers exhibit outstanding strength and stiffness properties in the longitudinal direction. Transverse to the fiber, the strengths and stiffnesses are many times lower. Accordingly, the principal stress directions can be used for optimal fiber alignment. The basic idea of this approach is that the shear stresses  $\tau$  become zero, while the normal stresses  $\sigma$  take extreme values, so that the longitudinal strength properties of the fibers can be used optimally [42]. In an infinitesimal material section, the shear stresses are tangential to the sides of the material section, while the normal stresses are normal to them. When the material section is rotated by angle  $\varphi$ , the shear stresses can be completely eliminated, while the normal stresses become maximum. In this case,  $\sigma_1 \geq \sigma_2$  as well as  $\sigma_1 \perp \sigma_2$ . The calculated stress states can be summarized in a matrix  $S$  [43]:

$$S = \begin{bmatrix} \sigma_{xx} & \tau_{xy} \\ \tau_{xy} & \sigma_{yy} \end{bmatrix} \quad (1)$$

According to [43] solving the eigenvalue problem with unit matrix  $I$  in Eq. (2) yields eigenvalues  $\sigma_{1,2}$  corresponding to Eq. (3), which correspond to the first and second principal stresses.

$$\det(S - \sigma I) = 0 \quad (2)$$

$$\sigma_{1,2} = \frac{\sigma_{xx} + \sigma_{yy}}{2} \pm \sqrt{\left(\frac{\sigma_{xx} - \sigma_{yy}}{2}\right)^2 + \tau_{xy}^2} \quad (3)$$

The directions of the principal stresses can be determined according to the following equation [44].

$$\tan(2\varphi^*) = \frac{2\tau_{xy}}{\sigma_{xx} - \sigma_{yy}} \quad (4)$$

The tangent function is periodic with  $\pi$ . Therefore, Eq. (4) with  $\varphi^*$  and  $\bar{\varphi}^* = \varphi^* + \pi/2$  provides the two mutually perpendicular principal directions [44]. According to Neuber [45], the directions of the first principal stress, described by the angle  $\varphi_1$ , can be determined directly with respect to the underlying coordinate system using Eq. (5) for plane stress problems.

$$\tan \varphi_1 = \frac{\tau_{xy}}{\sigma_{xx} - \sigma_2} \quad (5)$$

The use of Eq. (5) has the advantage that the angle  $\varphi_1$ , which is to be assigned to the first principal stress direction, can be calculated directly. Thus, the ambiguity is avoided when calculating  $\tan(2\varphi)$  from Eq. (4).

The principal stresses can be represented in the form of so-called trajectories, which are tangential to the principal stress directions at each point. In composite parts, these trajectories can be considered as load-adapted fiber paths that take into account the anisotropic fiber properties (see Fig. 3).

## 3 Materials and methods

In this section, the study design and methods used are presented. The approach used to generate the G-code for the principal stress-based fiber alignment is discussed, as well as the fabrication setup. In addition, the specimen design and the mechanical testing procedure are described.

### 3.1 Principal stress-based toolpath planning

A suitable method, which is also used in this work for the visualization and generation of the optimized fiber alignments, is the CAIO method. Moldenhauer presents in [41] a CAIO approach to visualize the principal stress trajectories in conventional finite element analysis (FEA) software. His mathematically proofed method is based on the following hypothesis [41]:

The isotherms of an orthotropic steady-state 2D thermal conduction problem with the thermal conductivities  $k_1$  and  $k_2$  are tangential to an arbitrarily prescribed direction field  $y' = f(x, y)$  provided that the local orientation of  $k_1$  follows the direction field  $y'$ , and perfect insulation exists perpendicular to this ( $k_2 = 0$ ).

The principal stress directions are direction fields which can be computed statically. The orthotropic thermal analysis

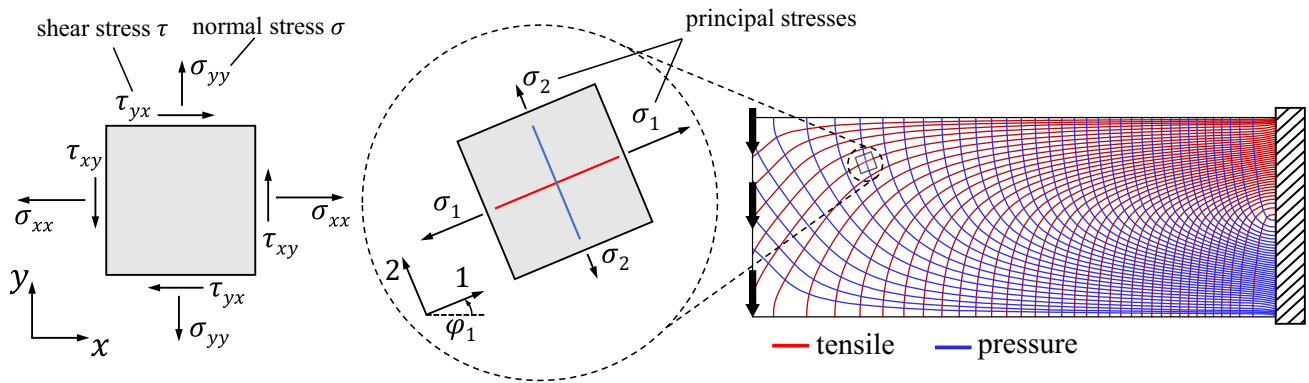


**Fig. 3** Principal stress trajectories of a beam subjected to bending with an infinitesimal material section

is independent from the static analysis and uses the principal stress directions as local systems for the conductivities  $k_1$  and  $k_2$ . Extreme orthotropic ratios ( $k_1/k_2$  for the first,  $k_2/k_1$  for the second principal stress direction, at least greater than  $1/1e^{-4}$ ) force the isotherms to follow the direction fields. According to the described procedure, a FE stress analysis is first performed in ABAQUS. The principal stress directions in the integration points of the finite elements of a 2D or 3D shell part are determined. The mutually perpendicular principal stress directions in the elements are transferred as local systems to a subsequent thermal FEA. The structural elements of the stress analysis are replaced by thermal elements without changing the node and element numbering. For common problems, two thermal boundary conditions in the form of heat sources with different temperatures in two nodes of the mesh are sufficient to visualize the isotherms over the entire mesh. They represent the principal stress trajectories. The placement of the two nodes with thermal boundary conditions is discussed in [41].

The result of this method is therefore a continuous temperature field in which the isotherms follow the principal stress directions. No iterations are necessary for the determination of the principal stress trajectories. With the help of post-processing software, any number of fiber trajectories can be generated from the continuous field at regular intervals or at defined points without any further calculation steps and output in the form of coordinates. The process flow is shown in Fig. 4.

Conventional slicing programs are not able to generate toolpaths for parts with complex fiber paths. Therefore, in this work, the 3D modeling software Rhinoceros3D version 7.0 with the visual programming environment Grasshopper was used to generate the toolpath. Since solid specimens were to be used for the investigations, infill patterns were generated for the inter-fiber spaces (see Fig. 5). A written program distinguished between fiber paths and intermediate areas within the layers. In the program used, the fiber paths

were first read in as coordinates and connected in the form of a curve. A specific path width was assigned to the fiber paths. The layer was then subdivided into the fiber paths with specific width and the intermediate spaces. Separate process parameters, such as extruder temperature, printing speed and print bed temperature, were defined for fiber paths and the intermediate infill. Furthermore, cutting commands were implemented for the fiber paths, which are located about 40 mm before the end points of the fiber path due to the distance between extruder and cutting unit. In addition, the G-code for unreinforced layers was generated, which was used for the first and last layers. The G-codes were then merged and sent to the printer.

### 3.2 Setup and materials

For the printing of the specimens, in this work a modified Renkforce RF2000 (Conrad Electronic SE, Hirschau, Germany) with a Duet3D control board with RepRap firmware (Duet3D Ltd., Peterborough, Great Britain) was used, which can be accessed by a browser interface (see Fig. 6). The printer's conventional printhead was replaced with a dual-extruder system from Markforged (Markforged Inc.), which is also used in its MarkTwo printer. Polyamide 6 (Nylon White) was used as the matrix filament and carbon fiber filament CFF from Markforged (Markforged, Inc., Watertown, MA, USA) was used as the reinforcing fiber. To prevent moisture absorption of the polyamide, the filament spools were stored in the airtight drying box PolyBox™ (Polymaker B.V., Shanghai, China) with a controlled relative humidity content of < 25%. The diameter of the nylon filament is 1.75 mm and the diameter of the continuous fiber filament is 0.4 mm. Approximately 1000 fibers are embedded in the continuous fiber filament. The fiber volume fraction has been measured in various investigations and varies between 32.8 and 34.5% [46, 47].

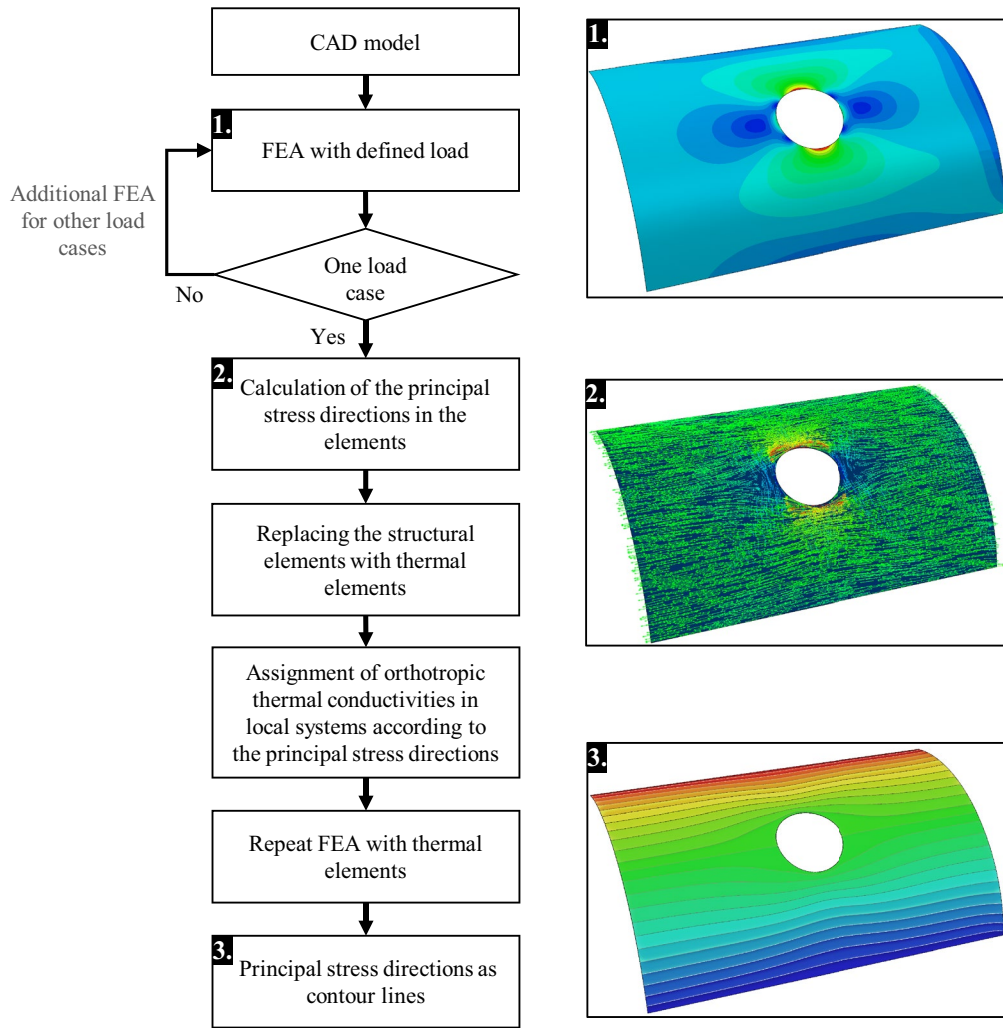


**Fig. 4** Flowchart of the CAIO method using orthotropic heat conduction as a numerical integrator with curved open-hole plate under tensile loading, according to Moldenhauer [41]

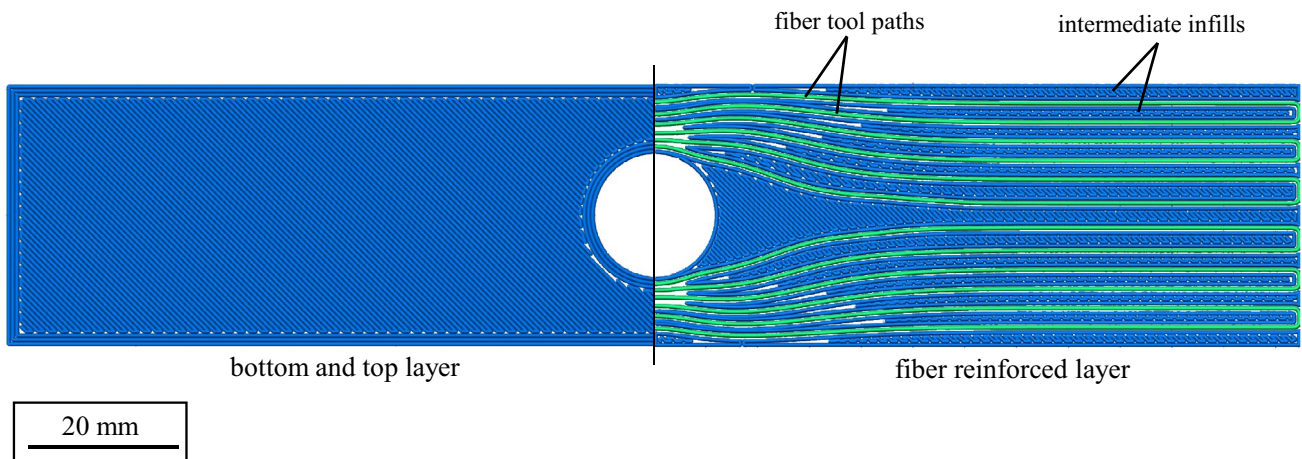


**Fig. 5** Exemplary infill pattern of the bottom and top layers and the fiber-reinforced layers

**Fig. 6** Renkforce RF2000 with Markforged Dual Extruder and Polymaker Polybox

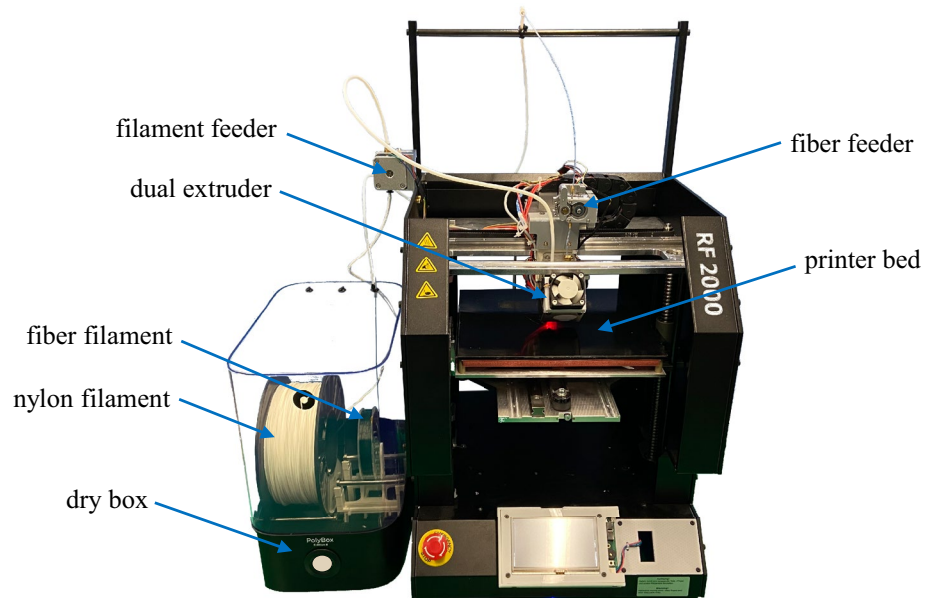


**Table 1** Process parameters for the fabrication of the specimens from nylon and carbon fiber

Parameter	Value	Unit
Extruder temperature	270	°C
Print bed temperature	90	°C
Nylon filament diameter	1.75	Mm
CF filament diameter	0.4	mm
Layer height fiber/nylon	0.125	mm
Bottom and top layers (nylon)	0.2	mm
Strand width (nylon)	0.4	mm
Fiber width	0.9	mm
Fill density	100	%
Nylon printing speed	40	mm/s
Fiber printing speed	8	mm/s
Infill angle	+45/-45	°

The specimens were fabricated from both fiber-reinforced and pure nylon layers. An overview of the process parameters used is shown in Table 1.

### 3.3 Specimen design and fabrication

Open-hole plates and flexural specimens were used as specimens to investigate the influence of optimized fiber orientations. The dimensions of the specimens are shown in Fig. 7. As a reference to the optimized specimens, fiber-reinforced specimens with unidirectional fiber orientation and comparable fiber volume fraction were additionally used. With the exception of the fiber orientation, the same process parameters as listed in Table 1 were used.

The simulation and calculation of the principal stress trajectories was performed according to the procedure described in Sect. 3.1. An element number of 38,400 was used for the flexural specimens and an element number of 47,460 was used for the open-hole plates. CPS4R elements are used as element type for the structural analysis, and DC2D4 elements are used for the thermal analysis. The G-code was generated using the developed program in Rhinoceros3D/Grasshopper. An exemplary process flow for a flexural specimen is shown in Fig. 8.

The generation of fiber paths for the open-hole plates was performed at constant distances in the direction of the first principal stress for both specimen types. In order to achieve a comparable fiber volume fraction  $V_f$ , this resulted in 12 fiber tracks per layer with a spacing of approx. 1.9 mm in the straight-line direction for the principal stress-based orientation and in 14 fiber tracks with a spacing of approx. 1.7 mm in the straight-line direction for the unidirectional fiber orientation (see Figs. 9, 10). The second principal stress direction was not considered for the open-hole plates.

The fiber orientation for the flexural specimens, on the other hand, is more complex due to the high relevance of both principal stress directions. Therefore, a distinction was made in the layers between the first and second principal stress directions. The complete filling of each layer allowed an alternating layer structure with alternating fiber orientations, each following the first or second principal stress direction (see Fig. 11a). The spacing between the fiber paths is subject to certain restrictions. On the one hand, the width of the deposited fiber strand has to be taken into account for the fiber orientation. Thus, the generated paths must have a distance of at least 0.9 mm to each other. Secondly, a minimum radius of curvature must not be undershot, otherwise

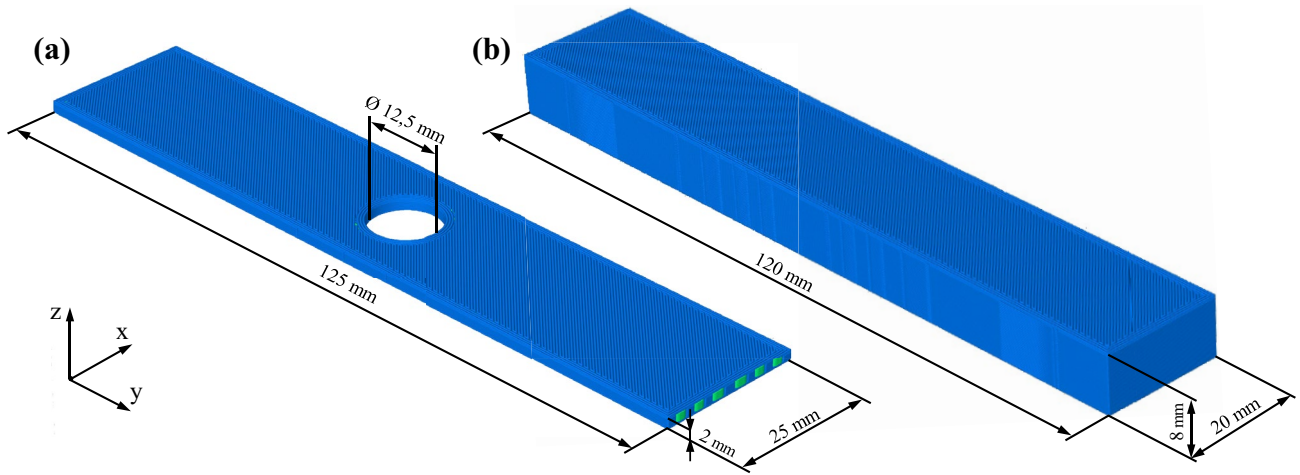


Fig. 7 Dimensions of the open-hole plate in (a) and the flexural specimen in (b)

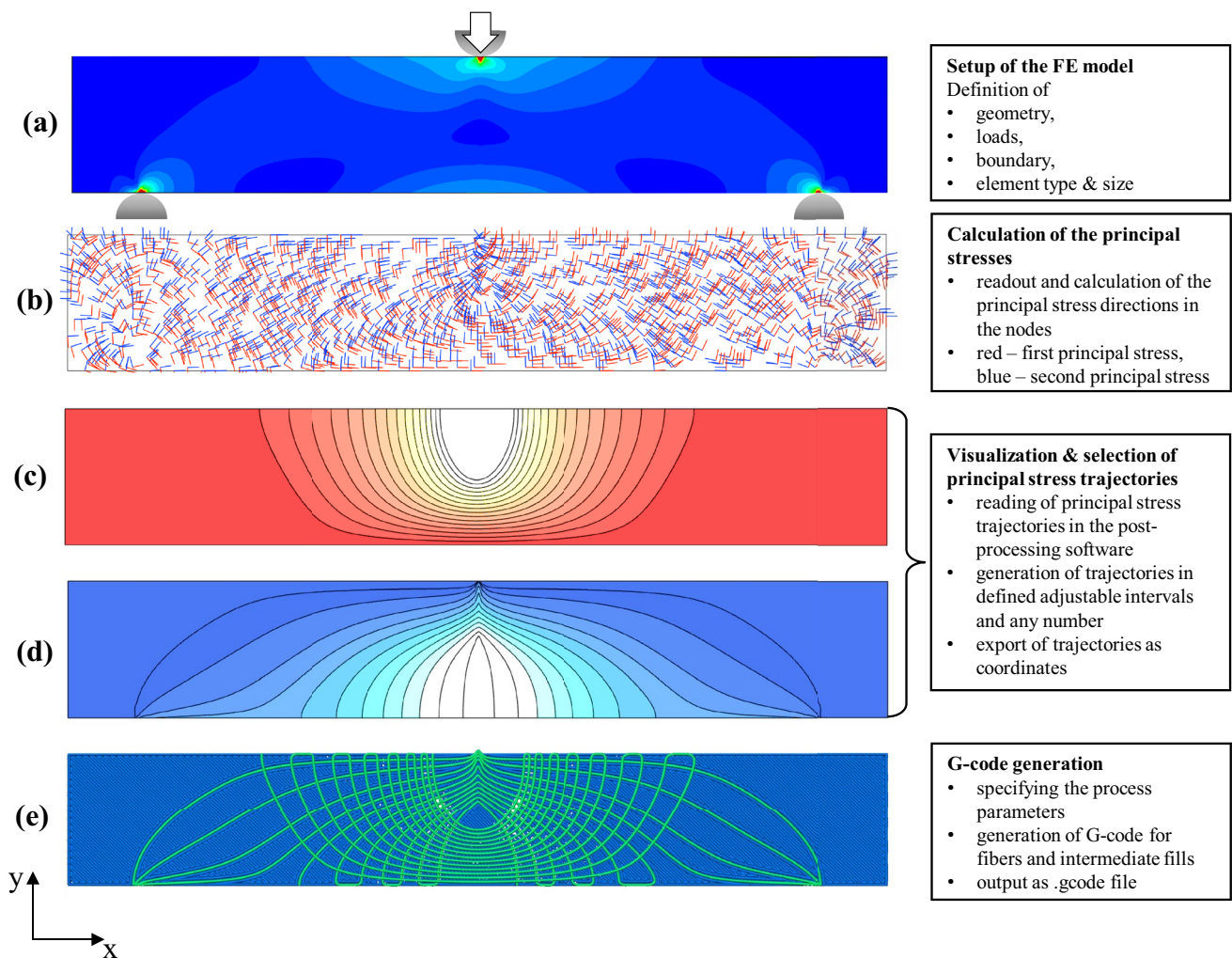
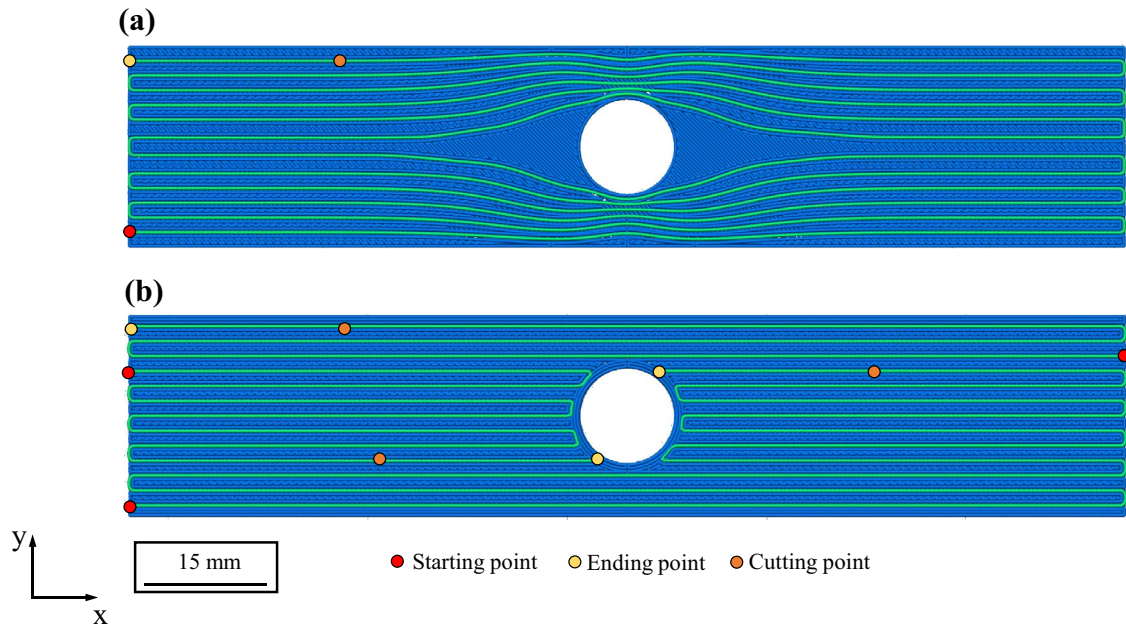


Fig. 8 Exemplary process flow for the generation of a stress-adapted infill pattern using the example of a flexural specimen; FE model in (a), principal stresses at right angles to each other in the nodal points

in (b), visualized principal stress trajectories in the post-processing software in (c, d), visualization of the G-code of the specimen in (e)



**Fig. 9** Comparison of fiber orientations for the open-hole plate along the principal stress trajectories in (a) and with unidirectional orientation in (b) with the starting, ending, and cutting positions

**Fig. 10** Optimized open-hole plate in (a) and open-hole plate with unidirectional fiber reinforcement in (b)



fiber breakage may occur. The exact minimum radius of curvature for the carbon fiber filament is not known. As an approximation, a radius of curvature corresponding to the width of the deposited fiber strand (0.9 mm) was used in this work. Taking these restrictions into account, the fiber curves were generated, which are shown in Figs. 11 and 12.

The underlying standard prescribes a minimum number of five specimens. This minimum number was taken into account for the present work. In order to reduce the production time of the flexural specimens, the middle part of the specimen was made of pure unreinforced thermoplastic with a height of 3.2 mm and layer thicknesses of 0.2 mm. The height of the fiber-reinforced layers was thus 4 mm in total with a layer height of 0.125 mm. The fabrication time

of an open-hole plate is about 30 min and the fabrication time of a flexural specimen is about 160 min.

For better comparability, the specimens were prepared with a fiber volume fraction as identical as possible. The fiber volume fraction describes the proportion of fibers in the total volume of the part and can be determined with the following formula [48]:

$$V_f = \frac{v_f}{v_c} \times 100 \% \tag{6}$$

where  $V_f$  is the fiber volume fraction,  $v_f$  is the total volume of the fibers and  $v_c$  is the total volume of the composite part. Due to the complex fiber characteristics in principal

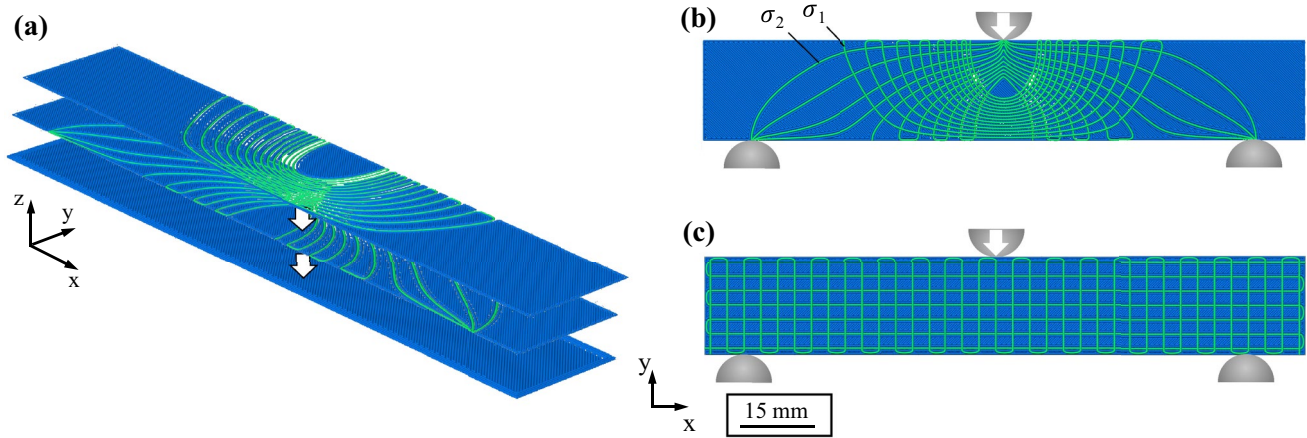


**Fig. 11** Schematic layered structure in (a) and comparison of fiber orientations for the flexural specimen along the principal stress direction in (b) and with unidirectional orientation in (c)

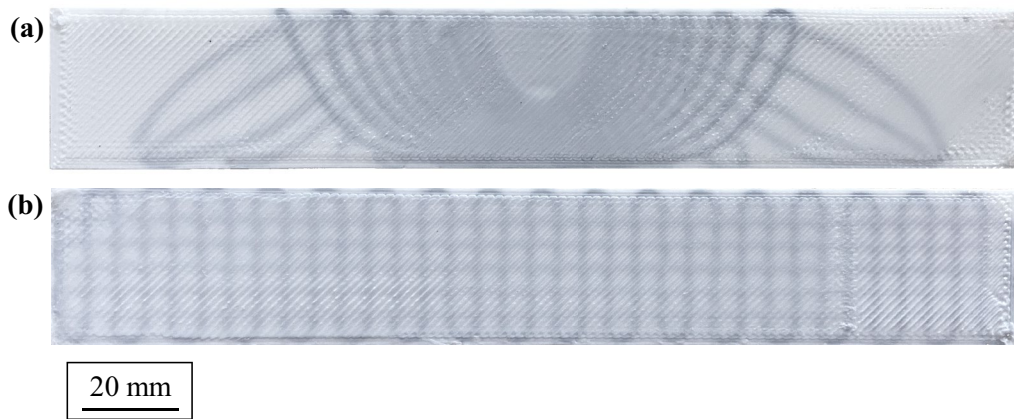


**Fig. 12** Fabricated optimized flexural specimen in (a) and unidirectional reinforced flexural specimen in (b)

**Table 2** Theoretically determined fiber volume fractions, subdivided by specimens and layers

Specimen/layer	Fiber volume fraction (%)
Open-hole plate (optimized)	9.5
Open-hole plate (unidirectional)	9.8
Flexural specimen (optimized)	5.4
Flexural specimen (optimized— $\sigma_1$ )	2.6
Flexural specimen (optimized— $\sigma_2$ )	2.8
Flexural specimen (unidirectional)	5.8
Flexural specimen (unidirectional— $0^\circ$ )	2.8
Flexural specimen (unidirectional— $90^\circ$ )	3.0

stress-based alignment compared to unidirectional fiber alignment, it was not possible to set an identical fiber volume fraction. Table 2 shows the respective theoretically

determined fiber volume fractions of the specimens with optimized and unidirectional fiber orientation. Furthermore, discrepancies between the different layer layouts of the flexural specimen were found. The fiber orientations corresponding to the first and second principal stresses or to a  $0^\circ$  and  $90^\circ$  infill pattern resulted in fiber volume fractions in the respective layers that could not be precisely adjusted. Therefore, Table 2 also lists the different fiber volume fractions, subdivided by layers. For the calculation, a fiber volume fractions of the fiber filament of 34% was assumed.

### 3.4 Tensile and flexural tests

The tensile tests were performed on the Zwick/Roell Zmart. Pro BZ1 universal testing machine (Zwick Roell, Ulm, Germany). The mean values of the measured values are given for the results. The specimen deformation was measured over the recorded crosshead travel. The test speed was 10 mm/

min. The 3-point bending test was performed to determine the characteristic values under bending load. The tests were performed on the same testing machine with identical testing speed. The machine force was recorded by load cell and the deformation by the crosshead travel of the testing machine. All mechanical tests were performed under the same environmental conditions.

A digital image correlation (DIC) system was used, which allows non-contact detection of deformations. The Aramis 5 M measuring system from GOM (Carl Zeiss GOM Metrology GmbH, Braunschweig, Germany) was used for this purpose. The system has two cameras and thus enables the measurement of two- and three-dimensional deformations. In order to measure the deformations of the specimens, stochastic patterns were applied to the surfaces of the specimens, which allowed the measurement system to optically

record the displacements. The images were taken at intervals of one second. The experimental setup is shown in Fig. 13.

The microstructure of the fracture surfaces of the flexural and tensile specimens were examined using a Zeiss Leo 1455VP scanning electron microscope (Carl Zeiss AG, Oberkochen, Germany).

## 4 Results

The results of the mechanical tests are described below. Figure 14 shows the force–displacement diagrams for the tensile and flexural tests for the optimized and unidirectional reinforced specimens. The average maximum forces with the corresponding standard deviations for the tensile and flexural tests are shown in Fig. 15.

**Fig. 13** Test setup of the tensile test with clamped tensile specimen with stochastic pattern and the digital image correlation system (DIC)

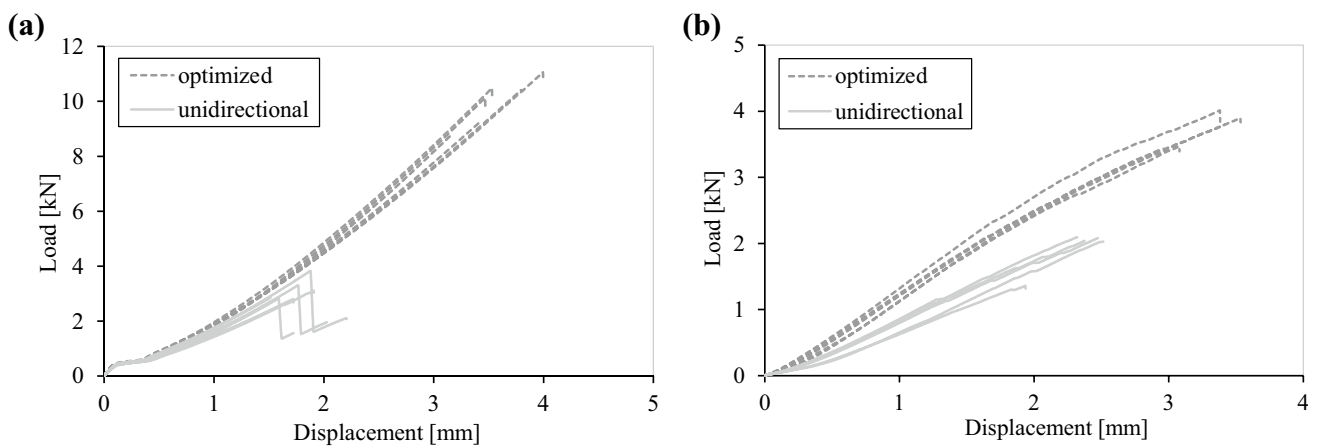
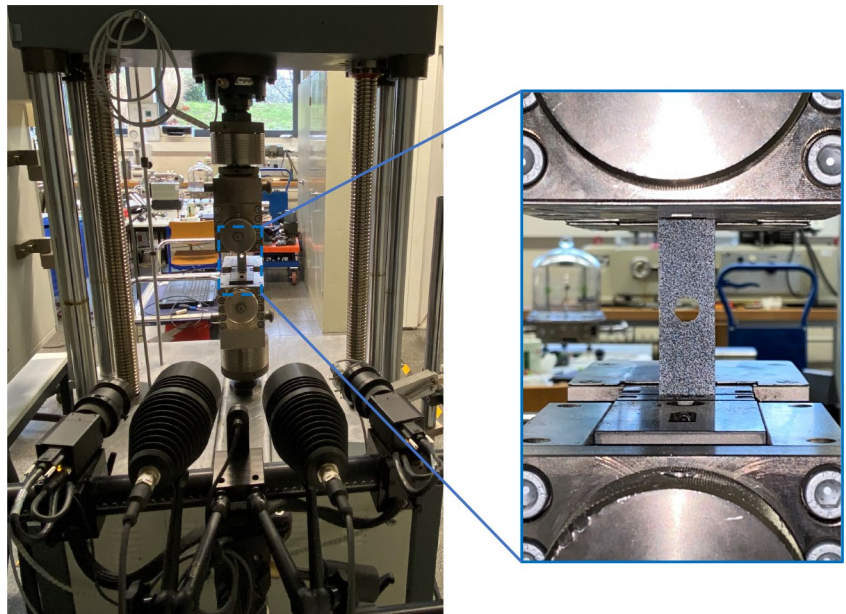
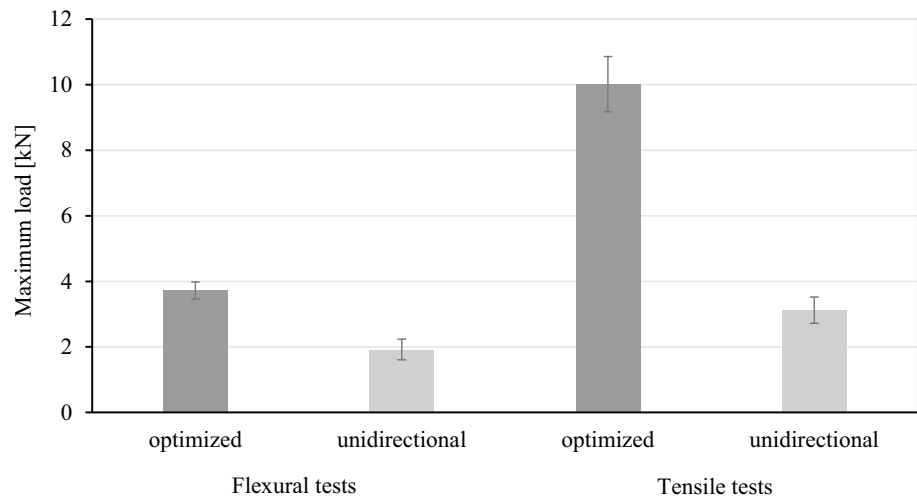


**Fig. 14** Force–displacement diagrams of the tensile tests in (a) and the flexural tests in (b)

**Fig. 15** Overview of the average maximum force of the tensile and flexural tests, subdivided into optimized and unidirectional reinforced specimens with the corresponding standard deviations



Considering the average values obtained (see Fig. 15), it becomes apparent that the optimized specimens absorb significantly higher peak loads in both test series. Compared with the unidirectional reinforced open-hole plates, the optimized open-hole plates with an average measured maximum force of approx. 10 kN have a peak load that is greater by a factor of 3. The optimized flexural specimens, on the other hand, withstand a maximum load of approx. 3.7 kN, a factor of 1.9 greater than the unidirectional reinforced specimens. As expected, all specimens exhibit brittle fracture. Three of the six unidirectional reinforced open-hole plates exhibit failure with multiple fractures (see Fig. 14a). This is due to the failure and fracture of individual fiber strands at short time intervals. In all three specimens, the first break is followed by a clearly visible drop in force with subsequent complete failure of the specimen.

The greater effects of principal stress-based fiber orientation on the mechanical properties of the tensile specimens compared with the flexural specimens are attributed to part weakening due to the hole. A significant amount of unidirectional fiber strands before and after the hole does not result in any increase in strength, which is also a primary criticism of conventional fiber orientation. In contrast, a fiber alignment based on the principal stress leads to a more uniform force distribution. It also results in simultaneous loading of all fiber strands and also reduces stress peaks at the weakened cross section. This is also evident from the measurements made using the digital image correlation system (Fig. 18).

Figures 16 and 17 show all broken tensile and flexural specimens. With the exception of one optimized specimen, which shows a deviating fracture pattern (see Fig. 16b, Specimen 1), all open-hole plates are fractured at the point with the smallest cross section. All unidirectional reinforced specimens have two broken pieces, while the optimized specimens are broken into an upper and lower

half, as well as several smaller broken pieces. The clearly visible damage around the hole is conspicuous, indicating that areas of high stress occur not only on the sides of the hole transverse to the load. This is also supported by the measurements using the digital image correlation system (see Fig. 18).

All fractured flexural specimens with unidirectional fiber orientation show an expected central fracture. In contrast, the optimized specimens show a completely different fracture pattern. All specimens show a fracture right of center with an approximately diagonal course through the specimen. The fracture occurs on the lower half along the second principal stress direction  $\sigma_2$  (compression) and on the upper half along the first principal stress direction  $\sigma_1$  (tension) (see also Fig. 20).

The results of the measurement using the digital image correlation system are shown in Fig. 18. The measurements were performed on each specimen. However, very similar deformations are observed in all measurements. Therefore, the measurements of the first specimen, respectively, at 50% and at 90% of the applied maximum load are presented as representative. Based on the measured deformations of the open-hole plates, the optimized specimens (Fig. 18a) show a significantly more homogeneous stress distribution at 50% of the maximum load compared with the unidirectional reinforced specimens (Fig. 18b). At 50% peak load, significant stress peaks transverse to the applied load can already be observed at the hole edges with unidirectional fiber orientation. These deformations increase progressively with increasing load. Above and below the hole, only very slight deformations are observed. At 90% load, the optimized specimens show a more homogeneous deformation over the surface, but exhibit increased deformations at the upper and lower sides of the hole. No compression is observed on the sides of the hole. The comparatively low strains at the weakest part cross section are remarkable. Nevertheless, even the

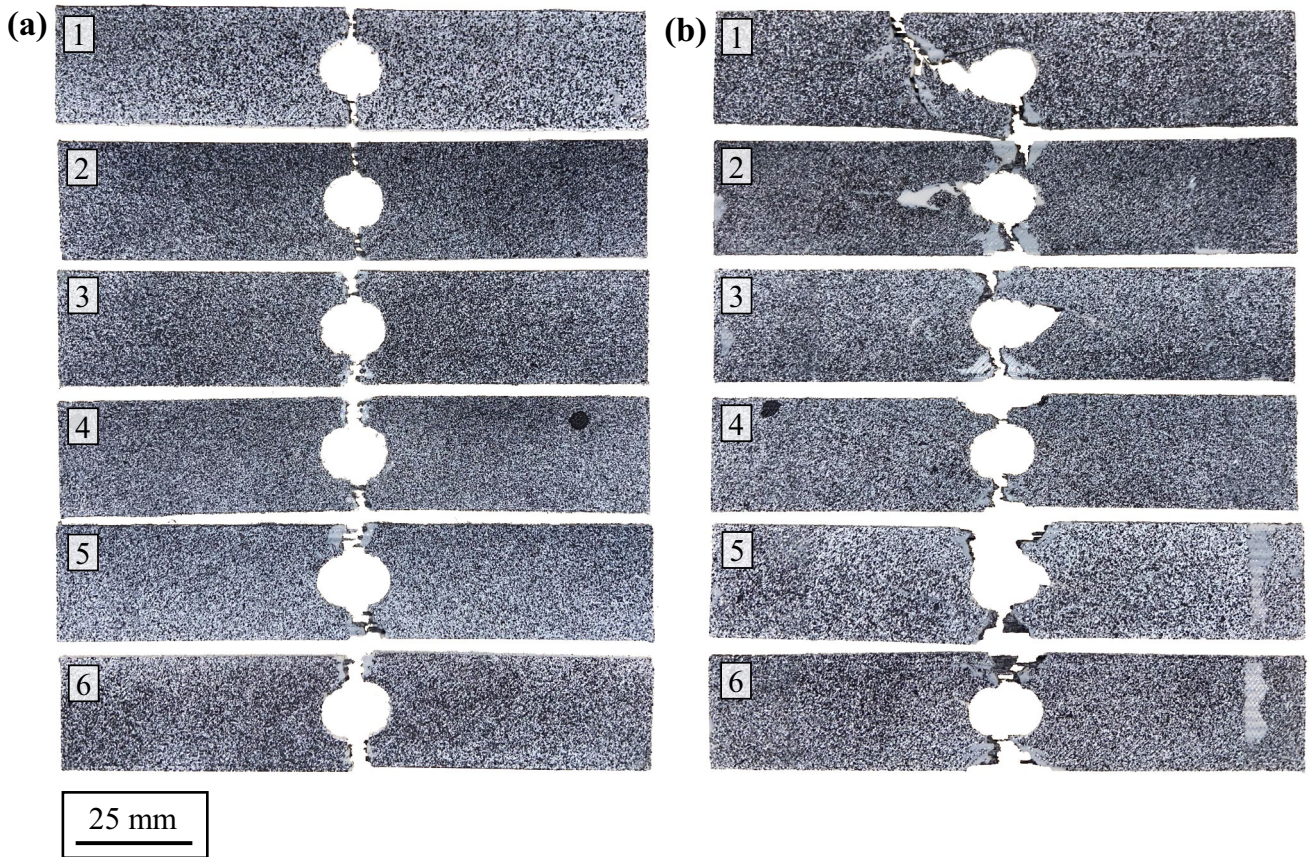


Fig. 16 Fractured tensile specimens with unidirectional fiber orientation in (a) and with optimized fiber orientation in (b)

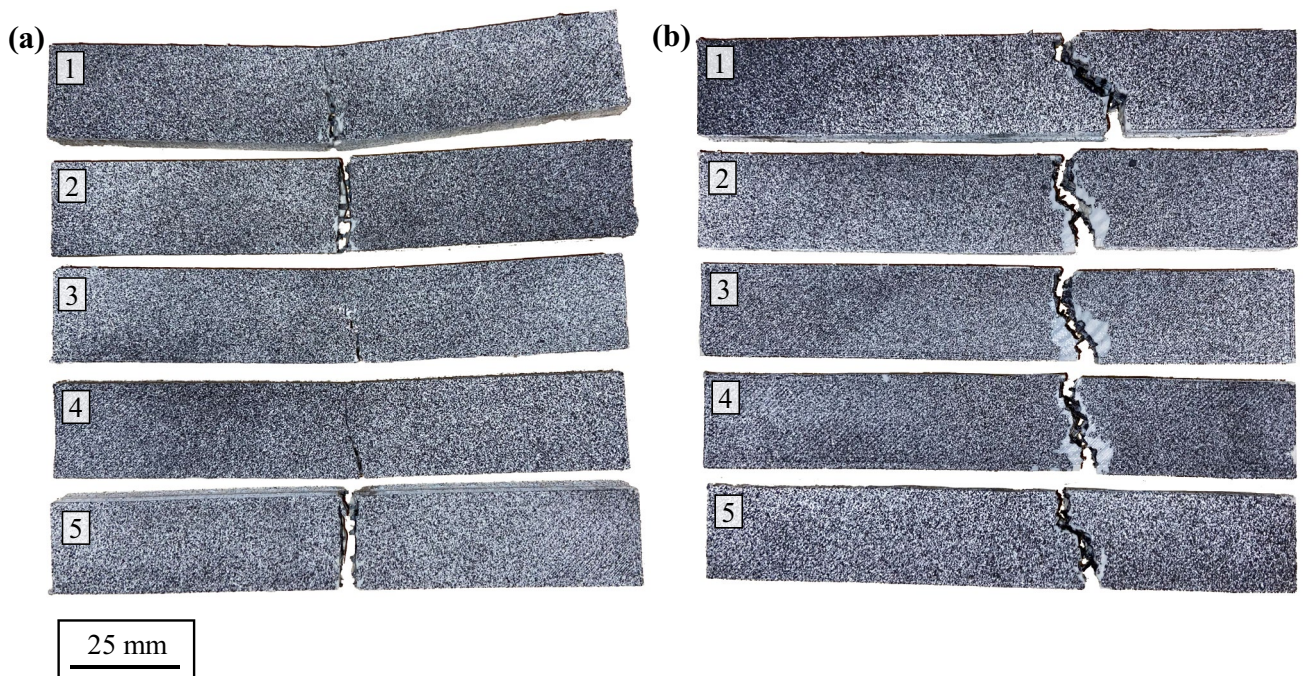
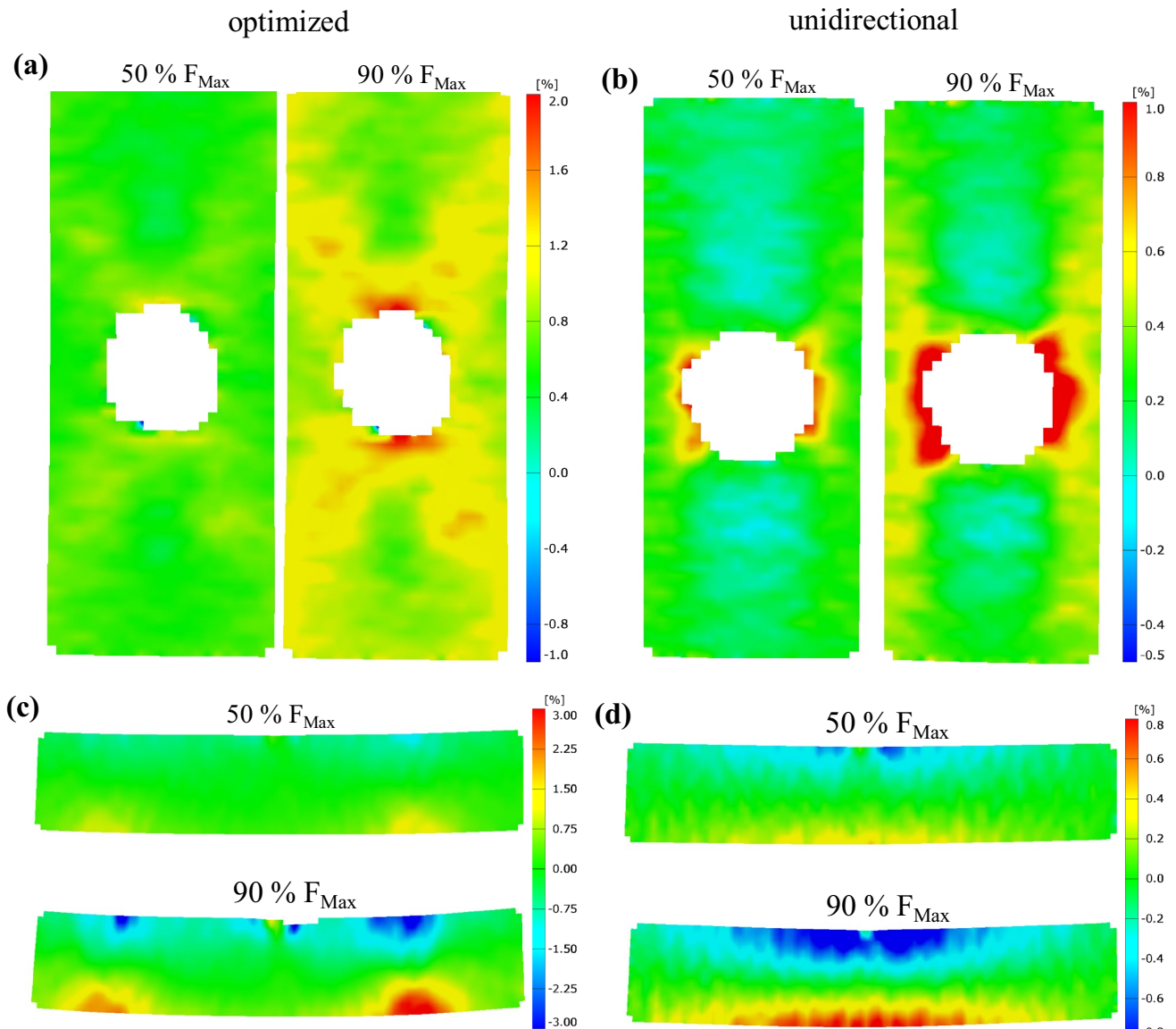


Fig. 17 Fractured flexural specimens with unidirectional fiber orientation in (a) and with optimized fiber orientation in (b)



**Fig. 18** Measured deformations using DIC for optimized tensile specimens in (a), unidirectional reinforced tensile specimens in (b), optimized flexural specimens in (c), and unidirectional reinforced flexural specimens in (d)

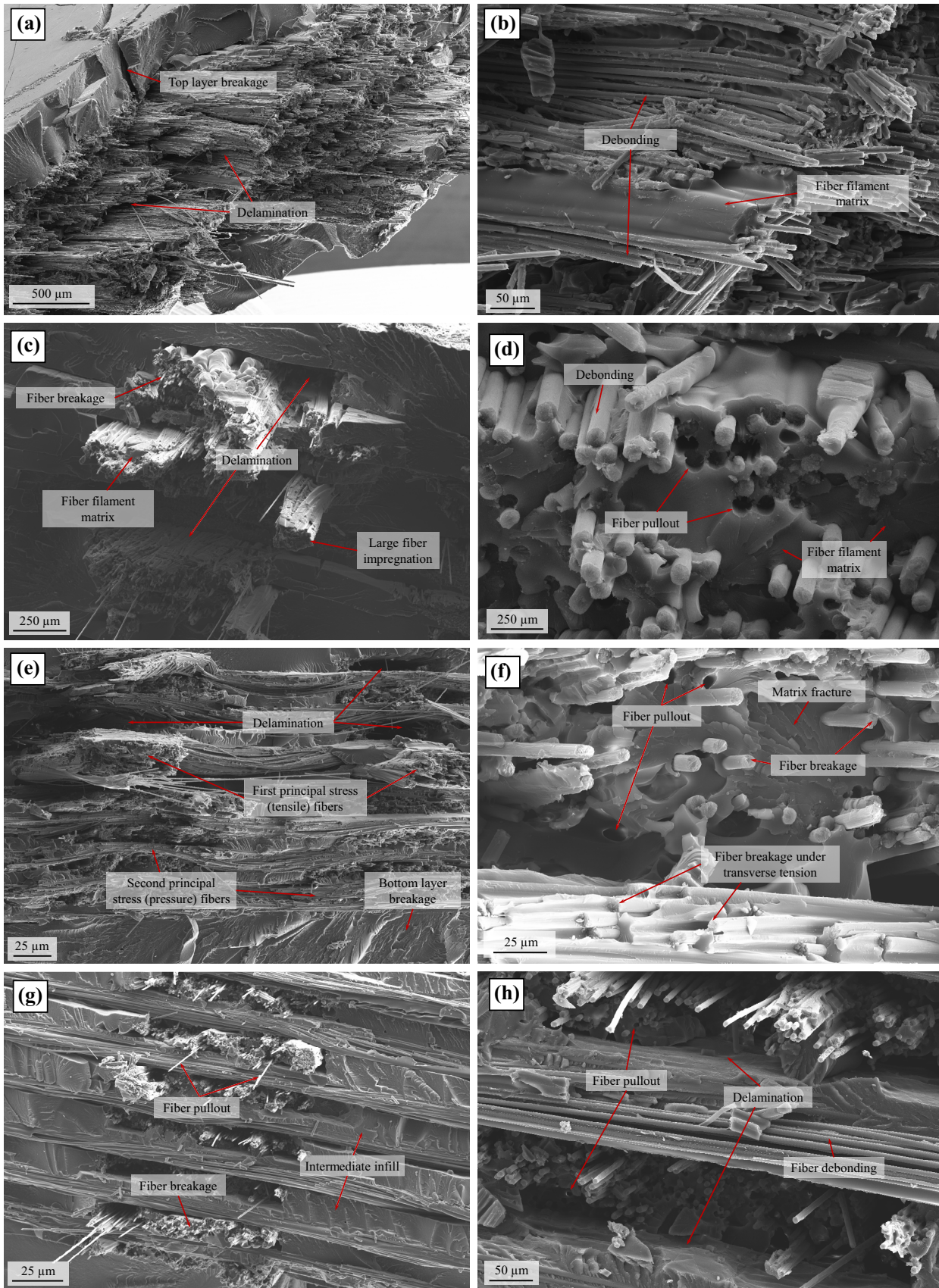
optimized open-hole plates show a dominant fracture pattern at the hole sides transverse to the load.

When comparing the measured deformations of the flexural specimens, very different deformations can be observed. While the flexural specimens with unidirectional fiber orientation (Fig. 18d) show deformations corresponding to the maximum bending moment, the optimized specimens show hardly any deformations in the middle area of the specimen (Fig. 18c). In the optimized specimens, the deformation shifts to the sides of the specimen, which is also expected from the off-center fractures of the specimens. The high fiber content in the most stressed areas in the center of the specimen prevents large deformation changes and leads to a

**Fig. 19** Microstructure of fractured cross sections of optimized tensile specimens in (a) and (b), unidirectional reinforced tensile specimens in (c, d), optimized flexural specimen in (e, f), and unidirectional reinforced flexural specimen in (g, h)

shift to the edges of the specimen with a lower relative fiber volume fraction.

The microstructure of the fracture surfaces was investigated using SEM images to determine the main failure mechanisms and to investigate possible differences between the fiber orientations. For this purpose, images were taken of both specimen types with optimized and unidirectional fiber orientations. The images are shown in Fig. 19.



All fracture surfaces show comparable failure mechanisms. The optimized tensile specimens are characterized by the significantly higher fiber content in the fracture surfaces of broken fiber strands. The unidirectionally reinforced tensile specimens show predominantly protruding or pulled-out fiber strands in the surrounding matrix. Based on the fracture surfaces of the optimized and unidirectional reinforced tensile specimens (Fig. 19a, c), delamination between the fiber layers is clearly visible. This indicates a low level of layer adhesion between the fiber strands. Within the layers, mainly exposed or vacancies caused by pulled out fibers can be seen, indicating a low interfacial adhesion between the matrix and the fibers embedded therein. In some cases, entire fiber bundles are present without surrounding matrix (see Fig. 19b). Debonding and delamination have also been identified by, e.g., in [16, 26–28] as major failure mechanisms in printed continuous fiber reinforced components. In some areas (e.g., Fig. 19d, f), non-uniform fiber embedding is also observed, with matrix-dominated areas and areas of high fiber density. This was also described in [49]. The layered structure is clearly observed in the flexural specimens (see Fig. 19e, g). The fracture surfaces of the flexural specimens also show delamination between the layers. The fracture surfaces of the unidirectionally reinforced flexural specimens (Fig. 19g, h) show that the fracture is at the level of the transversely embedded fiber strands. In this context, the transversely embedded fibers act as a weak point. The same behavior is also seen in the optimized bending specimens, where the fibers are aligned along the principal stress directions. On the tensile side of the specimens, the fracture

occurs in the direction of the second principal stress direction (compression). On the compressive side, however, the fracture occurs along the first principal stress direction (tension). The curved fiber strands therefore lead to a slanted fracture progression. The fracture path is illustrated in Fig. 20. The debonding, which can be observed in the tensile specimens even under tensile loading, is intensified by the transverse loading of the fiber strands. The inhomogeneity of the fiber strands promotes cracking and fracture of the specimen under transverse tension. Therefore, hardly any matrix around the adjacent transversely embedded fibers is visible at the fracture surface of the flexural specimens (see Fig. 19f, h).

## 5 Conclusion

In this work, a method was presented that allows the continuous fiber-reinforced additive manufacturing of parts with load-oriented fiber alignment. The fibers are aligned along the first and, if necessary, the second principal stress direction. A CAIO approach was chosen to calculate the principal stress trajectories. A developed program generates the G-code required for manufacturing based on the part geometry and the calculated trajectories. The use of a dual extruder allows the production of parts made of unreinforced thermoplastic with the possibility of local integration of continuous fiber strands.

Based on the presented method, tensile tests on carbon fiber reinforced open-hole plates and flexural tests were

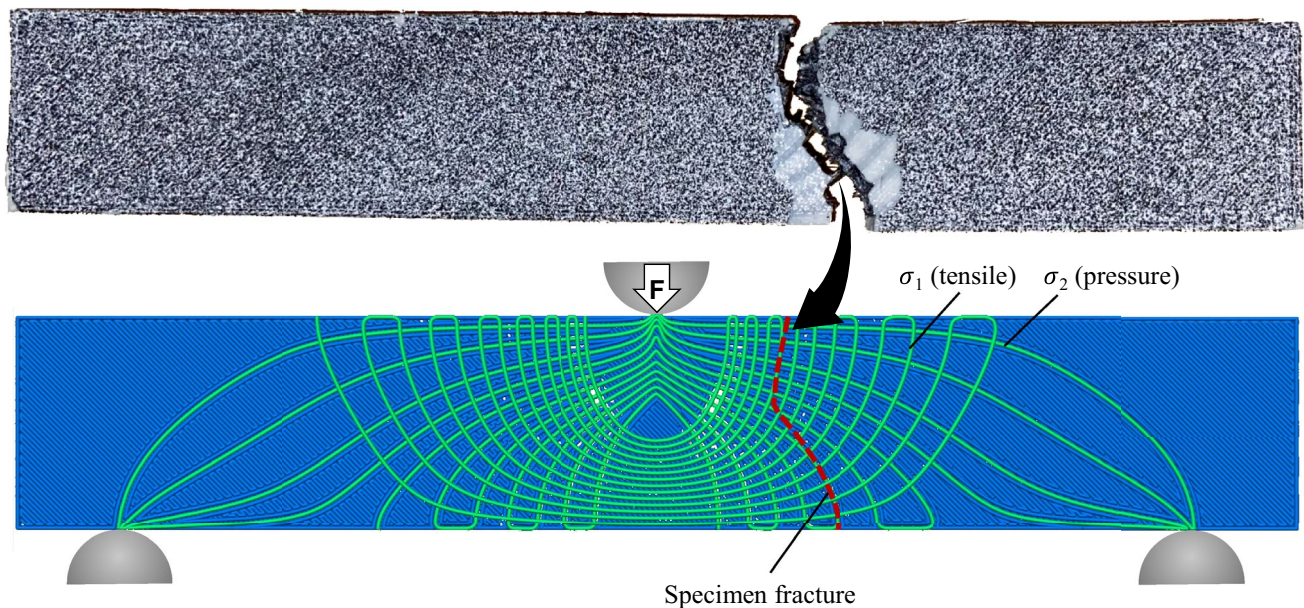


**Fig. 20** Fracture progression along the first principal stress direction for the lower half and along the second principal stress direction for the upper half of the flexural specimen

performed. The specimens were fabricated and tested with both principal stress-based and unidirectional fiber alignment. For the tensile specimens, only the first principal stress direction was considered, while for the flexural specimens both the first and second principal stress directions were considered. In this case, the slicing program allows an alternating layer structure with alternating fiber orientations. In order to better compare the tensile and flexural specimens with different fiber orientations, similar fiber volume fraction was used. During the mechanical tests, it was found that the principal stress-based orientation of the fibers led to a significant increase in the strength of the parts. The peak load of the optimized tensile specimens exceeded that of the tensile specimens with unidirectional fiber orientation by a factor of about 3. The optimized flexural specimens showed a peak load that was higher by a factor of 1.9 compared with flexural specimens and unidirectional fiber orientation. Based on measurements using digital image correlation, it was shown that a principal stress-based fiber orientation leads to a more homogeneous stress distribution. This results in a reduction in stress peaks, especially in weakened part cross sections.

The proposed process therefore makes it possible to significantly increase the strength of continuous fiber-reinforced and additively manufactured parts or to reduce the weight or fiber content while maintaining the same mechanical properties. In principle, the method is also useful for additively manufactured parts without fiber reinforcement, for example for additively manufactured lattice structures. In the context of fiber-reinforced parts, however, the stress-based fiber alignment is of particular importance. Since the fibers exhibit outstanding strength and stiffness properties in the longitudinal direction, but only very low strengths and stiffnesses transverse to the fiber orientation, minimization of the shear stresses is a target for improving the mechanical properties. This is made possible with principal stress-based fiber orientation. In future, principal stress-based fiber alignment using simulation-based calculations in slicing programs could lead to an increasing use of continuous fiber-reinforced material in the industry. It should be noted, however, that larger loads can only occur in one direction parallel to the build plane. In this context, processes must be developed in future that enable additive manufacturing of continuous fiber-reinforced parts with a fiber orientation in multiple spatial directions. Also, the improvement of the interfacial adhesion between fiber and matrix and the adhesion between the layers should be given special attention, since in this work it was shown that delamination and debonding are the main failure mechanisms.

**Supplementary Information** The online version contains supplementary material available at <https://doi.org/10.1007/s40964-022-00347-x>.

**Author contributions** Conceptualization was contributed by T.H.; methodology was contributed by T.H.; formal analysis was contributed by T.H., S.K., and S.G.; T.H. and J.D.M contributed to design and manufacturing of the test specimens; T.H. and J.-D. M. contributed to investigation; T.H. contributed to writing—original draft preparation; S.K., S.G. and N.W. contributed to writing—review and editing; T.H. contributed to visualization; G.K., N.W. and T.V. contributed to supervision; G.K., N.W. and T.V. contributed to project administration; G.K., N.W. and T.V. contributed to funding acquisition. All authors have read and agreed to the published version of the manuscript.

**Funding** Open Access funding enabled and organized by Projekt DEAL. Funded by the Ministry for Science and Culture of Lower Saxony (MWK), School for Additive Manufacturing SAM.

## Declarations

**Conflict of interest** The authors declare that they have no conflict of interest.

**Open Access** This article is licensed under a Creative Commons Attribution 4.0 International License, which permits use, sharing, adaptation, distribution and reproduction in any medium or format, as long as you give appropriate credit to the original author(s) and the source, provide a link to the Creative Commons licence, and indicate if changes were made. The images or other third party material in this article are included in the article's Creative Commons licence, unless indicated otherwise in a credit line to the material. If material is not included in the article's Creative Commons licence and your intended use is not permitted by statutory regulation or exceeds the permitted use, you will need to obtain permission directly from the copyright holder. To view a copy of this licence, visit <http://creativecommons.org/licenses/by/4.0/>.

## References

1. Gebhardt A (2016) Additive Fertigungsverfahren: Additive Manufacturing und 3D-Drucken für Prototyping—Tooling—Produktion, 5th edn. Hanser, München
2. Gibson I, Rosen D, Stucker B (2015) Additive manufacturing technologies: 3D printing, rapid prototyping and direct digital manufacturing, 2nd edn. Springer, New York
3. Mazurchevici A., Nedelcu D, Popa R (eds) (2020) Additive manufacturing of composite materials by FDM technology: a review. *Indian J Eng Mater Sci* 27:179–192
4. Ngo TD, Kashani A, Imbalzano G et al (2018) Additive manufacturing (3D printing): a review of materials, methods, applications and challenges. *Compos B Eng* 143:172–196. <https://doi.org/10.1016/j.compositesb.2018.02.012>
5. Mohan N, Senthil P, Vinodh S et al (2017) A review on composite materials and process parameters optimisation for the fused deposition modelling process. *Virtual Phys Prototyping* 12:47–59. <https://doi.org/10.1080/17452759.2016.1274490>
6. Bryll K, Piesowicz E, Szymański P et al (2018) Polymer composite manufacturing by FDM 3D printing technology. *MATEC Web Conf* 237:2006. <https://doi.org/10.1051/mateconf/201823702006>
7. Ning F, Cong W, Qiu J et al (2015) Additive manufacturing of carbon fiber reinforced thermoplastic composites using fused deposition modeling. *Compos B Eng* 80:369–378. <https://doi.org/10.1016/j.compositesb.2015.06.013>

8. Ferreira RTL, Amatte IC, Dutra TA et al (2017) Experimental characterization and micrography of 3D printed PLA and PLA reinforced with short carbon fibers. *Compos B Eng* 124:88–100. <https://doi.org/10.1016/j.compositesb.2017.05.013>
9. Torrado Perez AR, Roberson DA, Wicker RB (2014) Fracture surface analysis of 3D-printed tensile specimens of novel ABS-based materials. *J Fail Anal Prev* 14:343–353. <https://doi.org/10.1007/s11668-014-9803-9>
10. Ning F, Cong W, Hu Z et al (2017) Additive manufacturing of thermoplastic matrix composites using fused deposition modeling: a comparison of two reinforcements. *J Compos Mater* 51:3733–3742. <https://doi.org/10.1177/0021998317692659>
11. Naranjo-Lozada J, Ahuett-Garza H, Orta-Castañón P et al (2019) Tensile properties and failure behavior of chopped and continuous carbon fiber composites produced by additive manufacturing. *Addit Manuf* 26:227–241. <https://doi.org/10.1016/j.addma.2018.12.020>
12. Blok LG, Longana ML, Yu H et al (2018) An investigation into 3D printing of fibre reinforced thermoplastic composites. *Addit Manuf* 22:176–186. <https://doi.org/10.1016/j.addma.2018.04.039>
13. Prüß H, Vietor T (2015) Design for fiber-reinforced additive manufacturing. *J Mech Des*. <https://doi.org/10.1115/1.4030993>
14. Kuschmitz S, Schirp A, Busse J et al (2021) Development and processing of continuous flax and carbon fiber-reinforced thermoplastic composites by a modified material extrusion process. *Materials (Basel)* 14:2332. <https://doi.org/10.3390/ma14092332>
15. Matsuzaki R, Ueda M, Namiki M et al (2016) Three-dimensional printing of continuous-fiber composites by in-nozzle impregnation. *Sci Rep* 6:23058. <https://doi.org/10.1038/srep23058>
16. Tian X, Liu T, Yang C et al (2016) Interface and performance of 3D printed continuous carbon fiber reinforced PLA composites. *Compos A Appl Sci Manuf* 88:198–205. <https://doi.org/10.1016/j.compositesa.2016.05.032>
17. Tian X, Liu T, Wang Q et al (2017) Recycling and remanufacturing of 3D printed continuous carbon fiber reinforced PLA composites. *J Clean Prod* 142:1609–1618. <https://doi.org/10.1016/j.jclepro.2016.11.139>
18. Fischer A, Rommel S, Bauernhansl T (2013) New fiber matrix process with 3D fiber printer—a strategic in-process integration of endless fibers using fused deposition modeling (FDM). *Digit Prod Process Dev* 2013:167–175
19. Hu Q, Duan Y, Zhang H et al (2018) Manufacturing and 3D printing of continuous carbon fiber prepreg filament. *J Mater Sci* 53:1887–1898. <https://doi.org/10.1007/s10853-017-1624-2>
20. Goh GD, Dikshit V, Nagalingam AP et al (2018) Characterization of mechanical properties and fracture mode of additively manufactured carbon fiber and glass fiber reinforced thermoplastics. *Mater Des* 137:79–89. <https://doi.org/10.1016/j.matdes.2017.10.021>
21. Dickson AN, Barry JN, McDonnell KA et al (2017) Fabrication of continuous carbon, glass and Kevlar fibre reinforced polymer composites using additive manufacturing. *Addit Manuf* 16:146–152. <https://doi.org/10.1016/j.addma.2017.06.004>
22. Bettini P, Alitta G, Sala G et al (2017) Fused deposition technique for continuous fiber reinforced thermoplastic. *J Mater Eng Perform* 26:843–848. <https://doi.org/10.1007/s11665-016-2459-8>
23. Justo J, Távora L, García-Guzmán L et al (2018) Characterization of 3D printed long fibre reinforced composites. *Compos Struct* 185:537–548. <https://doi.org/10.1016/j.compstruct.2017.11.052>
24. Melenka GW, Cheung BK, Schofield JS et al (2016) Evaluation and prediction of the tensile properties of continuous fiber-reinforced 3D printed structures. *Compos Struct* 153:866–875. <https://doi.org/10.1016/j.compstruct.2016.07.018>
25. Kabir SMF, Mathur K, Seyam A-FM (2020) A critical review on 3D printed continuous fiber-reinforced composites: history, mechanism, materials and properties. *Compos Struct* 232:111476. <https://doi.org/10.1016/j.compstruct.2019.111476>
26. Luo M, Tian X, Shang J et al (2019) Impregnation and interlayer bonding behaviours of 3D-printed continuous carbon-fiber-reinforced poly-ether-ether-ketone composites. *Compos A Appl Sci Manuf* 121:130–138. <https://doi.org/10.1016/j.compositesa.2019.03.020>
27. Liu T, Tian X, Zhang M et al (2018) Interfacial performance and fracture patterns of 3D printed continuous carbon fiber with sizing reinforced PA6 composites. *Compos A Appl Sci Manuf* 114:368–376. <https://doi.org/10.1016/j.compositesa.2018.09.001>
28. Caminero MA, Chacón JM, García-Moreno I et al (2018) Interlaminar bonding performance of 3D printed continuous fibre reinforced thermoplastic composites using fused deposition modeling. *Polym Test* 68:415–423. <https://doi.org/10.1016/j.polymertesting.2018.04.038>
29. Deutsches Institut für Normung e. V (1983) DIN 66025-1: Programm Aufbau für numerisch gesteuerte Arbeitsmaschinen. Beuth Verlag GmbH, Berlin
30. Girnth S, Koopmann J, Klawitter G et al (2019) 3D hybrid-material processing in selective laser melting: implementation of a selective coating system. *Prog Addit Manuf* 4:399–409. <https://doi.org/10.1007/s40964-019-00082-w>
31. Markforged Inc. (2022) Carbon Fiber Composite 3D Printer: Markforged Mark Two. <https://markforged.com/3d-printers/mark-two>. Accessed 16 Mar 2022
32. Anisoprint LLC (2022) Desktop Anisoprinting. <https://anisoprint.com/>. Accessed 08 Feb 2022
33. Markforged Inc. (2022) Eiger 3D Printing Software | Markforged. <https://markforged.com/software>. Accessed 16 Mar 2022
34. Anisoprint (2022) Aura | Anisoprint. <https://anisoprint.com/aura/>. Accessed 10 Feb 2022
35. Zhang H, Yang D, Sheng Y (2018) Performance-driven 3D printing of continuous curved carbon fibre reinforced polymer composites: a preliminary numerical study. *Compos B Eng* 151:256–264. <https://doi.org/10.1016/j.compositesb.2018.06.017>
36. Malakhov AV, Polilov AN (2016) Design of composite structures reinforced curvilinear fibres using FEM. *Compos A Appl Sci Manuf* 87:23–28. <https://doi.org/10.1016/j.compositesa.2016.04.005>
37. Malakhov AV, Polilov AN, Li D et al (2021) Increasing the bearing capacity of composite plates in the zone of bolted joints by using curvilinear trajectories and a variable fiber volume fraction. *Mech Compos Mater* 57:287–300. <https://doi.org/10.1007/s11029-021-09954-1>
38. Sugiyama K, Matsuzaki R, Malakhov AV et al (2020) 3D printing of optimized composites with variable fiber volume fraction and stiffness using continuous fiber. *Compos Sci Technol* 186:107905. <https://doi.org/10.1016/j.compscitech.2019.107905>
39. Li N, Link G, Wang T et al (2020) Path-designed 3D printing for topological optimized continuous carbon fibre reinforced composite structures. *Compos B Eng* 182:107612. <https://doi.org/10.1016/j.compositesb.2019.107612>
40. Hou Z, Tian X, Zhang J et al (2021) Optimization design and 3D printing of curvilinear fiber reinforced variable stiffness composites. *Compos Sci Technol* 201:108502. <https://doi.org/10.1016/j.compscitech.2020.108502>
41. Moldenhauer H (2018) Integration of direction fields with standard options in finite element programs. *MCA* 23:24. <https://doi.org/10.3390/mca23020024>
42. Henning F, Moeller E (2020) *Handbuch Leichtbau: Methoden, Werkstoffe, Fertigung*, 2nd edn. Hanser, München
43. Kessel S, Fröhling D (2012) *Technische Mechanik: Zweisprachiges Lehrbuch zu Grundlagen der Mechanik fester Körper*: bilingual textbook on the fundamentals of solid mechanics/

- Siegfried Kessel ; Dirk Fröhling = Engineering mechanics, 2., überarb. Aufl. Studium. Springer Vieweg, Wiesbaden
44. Schnell W, Gross D, Hauger W (1990) Elastostatik, 3. Aufl. Springer-Lehrbuch, Bd. 2. Springer, Berlin
  45. Neuber H (1971) Technische Mechanik Methodische Einführung: Zweiter Teil Elastostatik und Festigkeitslehre. Springer, Berlin
  46. Van Der Klift F, Koga Y, Todoroki A et al (2016) 3D printing of continuous carbon fibre reinforced thermo-plastic (CFRTP) tensile test specimens. OJCM 06:18–27. <https://doi.org/10.4236/ojcm.2016.61003>
  47. Dutra TA, Ferreira RTL, Resende HB et al (2019) Mechanical characterization and asymptotic homogenization of 3D-printed continuous carbon fiber-reinforced thermoplastic. J Braz Soc Mech Sci Eng. <https://doi.org/10.1007/s40430-019-1630-1>
  48. Macherauch E, Zoch H-W (eds) (2019) Praktikum in Werkstoffkunde: 100 ausführliche Versuche aus wichtigen Gebieten der Werkstofftechnik, 13, überarbeitete und, erweiterte. Springer Vieweg, Wiesbaden, Heidelberg
  49. Chabaud G, Castro M, Denoual C et al (2019) Hygromechanical properties of 3D printed continuous carbon and glass fibre reinforced polyamide composite for outdoor structural applications. Addit Manuf 26:94–105. <https://doi.org/10.1016/j.addma.2019.01.005>

**Publisher's Note** Springer Nature remains neutral with regard to jurisdictional claims in published maps and institutional affiliations.